

Instability of Agyrotropic Electron Beams near the Electron Diffusion Region

D. B. Graham,¹ Yu. V. Khotyaintsev,¹ A. Vaivads,¹ C. Norgren,^{1,2} M. André,¹ J. M. Webster,³ J. L. Burch,⁴ P.-A. Lindqvist,⁵ R. E. Ergun,⁶ R. B. Torbert,⁷ W. R. Paterson,⁸ D. J. Gershman,^{8,9} B. L. Giles,⁸ W. Magnes,¹⁰ and C. T. Russell¹¹

¹Swedish Institute of Space Physics, Uppsala SE-75121, Sweden

²Department of Physics and Astronomy, Uppsala University, Uppsala SE-75121, Sweden

³Department of Physics and Astronomy, Rice University, Houston, Texas 77005, USA

⁴Southwest Research Institute, San Antonio, Texas 78238, USA

⁵Space and Plasma Physics, School of Electrical Engineering, KTH Royal Institute of Technology, Stockholm SE-11428, Sweden

⁶Laboratory of Atmospheric and Space Physics, University of Colorado, Boulder, Colorado 80303, USA

⁷Space Science Center, University of New Hampshire, Durham, New Hampshire 03824, USA

⁸NASA Goddard Space Flight Center, Greenbelt, Maryland 20771, USA

⁹Department of Astronomy, University of Maryland, College Park, Maryland 20742, USA

¹⁰Space Research Institute, Austrian Academy of Sciences, Graz 8042, Austria

¹¹Department of Earth and Space Sciences, University of California, Los Angeles, California 90095, USA

(Received 3 December 2016; published 13 July 2017)

During a magnetopause crossing the Magnetospheric Multiscale spacecraft encountered an electron diffusion region (EDR) of asymmetric reconnection. The EDR is characterized by agyrotropic beam and crescent electron distributions perpendicular to the magnetic field. Intense upper-hybrid (UH) waves are found at the boundary between the EDR and magnetosheath inflow region. The UH waves are generated by the agyrotropic electron beams. The UH waves are sufficiently large to contribute to electron diffusion and scattering, and are a potential source of radio emission near the EDR. These results provide observational evidence of wave-particle interactions at an EDR, and suggest that waves play an important role in determining the electron dynamics.

DOI: 10.1103/PhysRevLett.119.025101

Magnetic reconnection is a fundamental process in plasmas, which transforms magnetic field energy into particle energy by reconfiguring the magnetic field topology [1]. The most general form of reconnection is asymmetric reconnection, where the reconnecting plasmas have distinct properties (e.g., at the Earth's magnetopause). The key region inside of which the magnetic fields reconnect is the electron diffusion region (EDR). There electrons violate the frozen in condition; i.e., they no longer follow the convective motion of the magnetic field, and electrons from different regions can mix. The processes occurring within EDRs are not fully understood, but are characterized by agyrotropic electron distributions [2–4]. Simulations show that these distributions are often crescent shaped and centered around the $\mathbf{E} \times \mathbf{B}$ direction. In simulations of asymmetric reconnection these distributions were found on the low-density side of the X line [5,6]. The Magnetospheric Multiscale (MMS) mission has observed such electron crescents in or near EDRs at the Earth's magnetopause [7,8], confirming these predictions.

Waves and wave-particle interactions are thought to play a crucial role in reconnection. Waves are a possible source of anomalous resistivity and particle diffusion, potentially enabling magnetic fields to reconnect. Previous observations show that a variety of waves can be generated by reconnection, e.g., upper-hybrid (UH) or Langmuir, electron cyclotron, lower-hybrid, whistler, and electrostatic solitary waves [9–18]. However, most of the reported wave observations

were made well outside the EDR. The generation and role of waves in or near EDRs has also been difficult to study in simulations because of the reduced separations between characteristic electron scales, such as the Debye length λ_D , electron inertial length, and electron thermal gyroradius ρ_e , employed to make simulations feasible. This reduced scale separation can suppress wave activity in the EDR [19], making EDRs seem laminar, whereas in nature EDRs may be turbulent. Similarly, the two-dimensional geometries employed in most simulations suppress waves propagating in the out-of-plane direction. As simulations are very challenging, the best progress can be achieved using *in situ* observations. In particular, the MMS spacecraft were specifically designed to resolve particles and fields at electron scales [20], enabling the role of waves in EDRs to be investigated.

In this Letter we investigate an EDR observed by the MMS mission at the Earth's magnetopause on December 14, 2015 near the subsolar point [21,22]. We present the first observational evidence of electrostatic wave generation by agyrotropic electron beams near an EDR. We use magnetic field \mathbf{B} data from the fluxgate magnetometer [23], electric field \mathbf{E} data from the electric field double probes [24,25], and particle data from the fast plasma investigation [26]. All data are presented in high-resolution burst mode. We present vector data in LMN coordinates based on minimum variance analysis (MVA) of \mathbf{B} from MMS1 over the magnetopause crossing, unless otherwise stated.

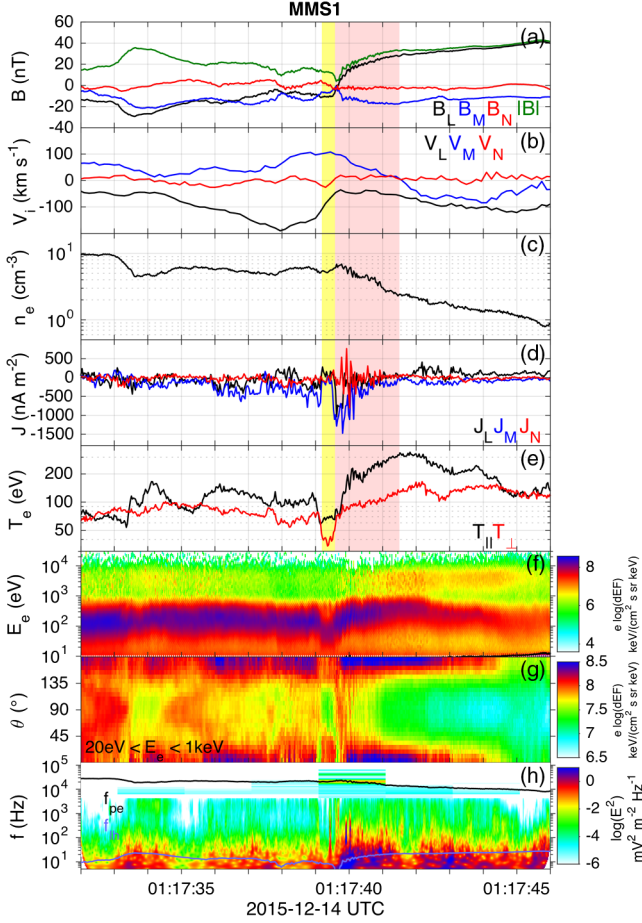


FIG. 1. Magnetopause crossing observed by MMS1. (a) \mathbf{B} . (b) \mathbf{V}_i . (c) n_e . (d) \mathbf{J} calculated from particle moments. (e) Electron T_{\parallel} and T_{\perp} . (f) Electron differential energy flux. (g) Electron pitch-angle distribution. (h) Spectrogram of \mathbf{E} (the black and blue lines are f_{pe} and f_{lh}). The yellow and red shaded regions indicate the EDR and magnetosheath inflow, and magnetospheric inflow region, respectively.

Here $\mathbf{L} = [0.14, -0.56, 0.81]$ is the reconnecting field direction, $\mathbf{M} = [-0.53, -0.74, -0.42]$ is the out-of-plane direction, and $\mathbf{N} = [0.84, -0.37, -0.40]$ is the normal direction in geocentric solar ecliptic coordinates.

Figure 1 provides an overview of the magnetopause crossing observed by MMS1. The crossing from the magnetosheath to the magnetosphere is characterized by a reversal in B_L , a relatively small guide field $B_M < 0$ [Fig. 1(a)], and southward ion outflow \mathbf{V}_i [Fig. 1(b)]. MMS1 enters the outflow region at 01:17:33 universal time (UT) where the electron number density n_e decreases [Fig. 1(c)]. Then, at 01:17:39 UT MMS1 enters the magnetosheath inflow region and EDR close to the X line—here the electron temperature T_e decreases rapidly, such that the perpendicular temperature T_{\perp} decreases below the magnetosheath T_{\perp} , while the parallel temperature T_{\parallel} becomes comparable to the magnetosheath value [Fig. 1(e)]. This temperature decrease is also seen in the

electron energy flux [Fig. 1(f)]. At 01:17:40 UT MMS1 crosses the X line, where $|\mathbf{B}|$ is minimal and $T_{\parallel} \approx T_{\perp}$, into the magnetospheric inflow region. Near the magnetopause (red-shaded region) we observe a large out-of-plane current density J_M , n_e gradient, and large T_{\parallel} , seen as the enhancement in the electron fluxes parallel and antiparallel to \mathbf{B} in Fig. 1(g). These features are consistent with magnetopause reconnection [27]. The fluctuations in J_N , \mathbf{B} , and n_e are consistent with lower-hybrid drift waves, which develop on the low n_e side of the X line [17,28–30], and are seen in the \mathbf{E} spectrogram around the lower-hybrid frequency f_{lh} [Fig. 1(h)]. We observe agyrotropic electron distributions over the entire yellow-shaded region in Fig. 1, indicating close proximity to the EDR. Here, we see a large enhancement in \mathbf{E} power at the electron plasma frequency f_{pe} .

Figures 2(a)–2(c) provide an overview of the EDR from MMS1, showing \mathbf{B} , the perpendicular and parallel components of the electron velocity, \mathbf{V}_{\perp} and \mathbf{V}_{\parallel} , and the agyrotropy measures \sqrt{Q} defined using Eq. (6) of Ref. [31], and $A\phi_e/2 = (P_{\perp \max} - P_{\perp \min}) / (P_{\perp \max} + P_{\perp \min})$ [2], where $P_{\perp \max}$ and $P_{\perp \min}$ are the maximum and minimum components of the electron pressure perpendicular to \mathbf{B} in the diagonal of the pressure tensor. For $A\phi_e/2$ we rotate the pressure tensor into field-aligned coordinates, such that $P_{\perp \max}$ and $P_{\perp \min}$ are most unequal. The primary difference between the measures is that $A\phi_e/2$ only considers agyrotropy in the plane perpendicular to \mathbf{B} , while \sqrt{Q} measures the full agyrotropy using all components of the electron pressure tensor \mathbf{P}_e . Both \sqrt{Q} and $A\phi_e/2$ peak near the X line, where B_L reverses direction and $|\mathbf{B}|$ is minimal, on the magnetosheath side. The fact that \sqrt{Q} and $A\phi_e/2$ peak when $B_L < 0$, suggests an EDR crossing [6], rather than a magnetospheric separatrix crossing, where significant agyrotropies may also develop [3]. The enhanced agyrotropies are due to electron distributions consisting of a low T_e core population with $T_{\parallel} > T_{\perp}$ and an electron beam or crescent propagating approximately perpendicular to \mathbf{B} . In the yellow-shaded region we observe low-density electron beams, shown in Figs. 2(f) and 2(g) in the plane perpendicular to \mathbf{B} . The distribution in Fig. 2(g) corresponds to the maximum \sqrt{Q} and $A\phi_e/2$. These beams propagate perpendicular to \mathbf{B} close to the out-of-plane direction, and are responsible for the enhanced \sqrt{Q} and $A\phi_e/2$. In the purple-shaded region closer to the X line we observe denser crescents [Fig. 2(h)], which rapidly increase in density toward the X line. Here, $A\phi_e/2$ significantly decreases, while \sqrt{Q} remains relatively large, indicating agyrotropy oblique, rather than perpendicular, to \mathbf{B} . At the X line the distributions remain agyrotropic but no clear crescents are observed. Figure 2(i) shows an electron distribution in the magnetospheric inflow region close to the X line. A crescentlike population is found, as expected from simulations [5,6], although the agyrotropy remains relatively small.

Both the beam and crescent distributions are distinct from the core, allowing us to estimate the beam velocity v_b and

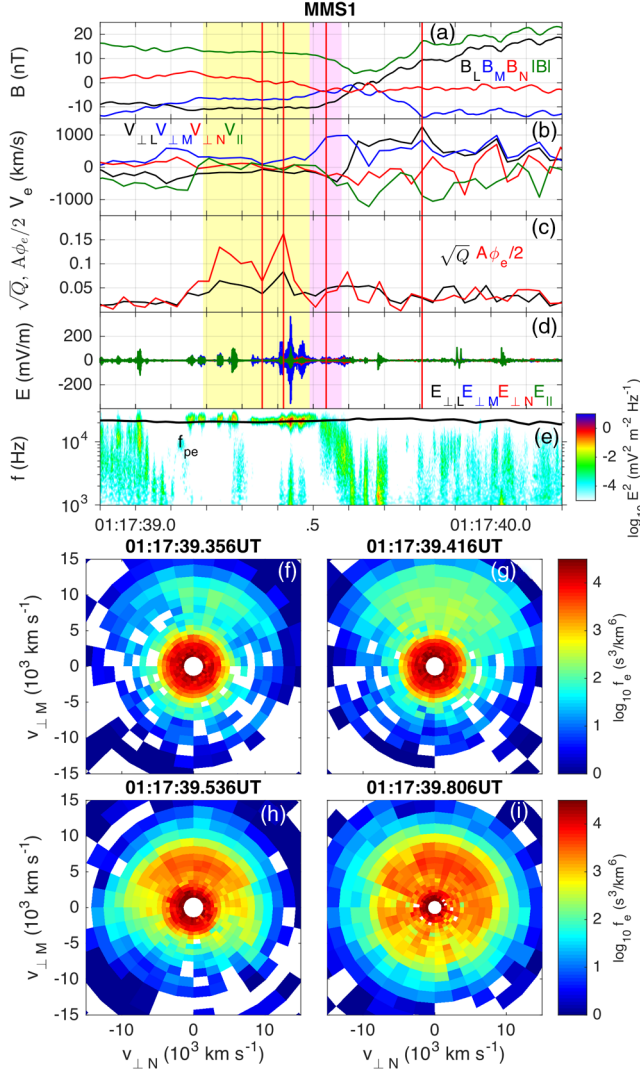


FIG. 2. EDR observed by MMS1. (a) \mathbf{B} . (b) Perpendicular and parallel components of \mathbf{V}_e . (c) Agyrotropy measures \sqrt{Q} and $A\phi_e/2$. (d) Perpendicular and parallel components of the high-frequency \mathbf{E} . (e) Spectrogram of \mathbf{E} . (f)–(i) Electron distributions at times indicated by the vertical red lines in (a)–(d) in the $\mathbf{N}_\perp - \mathbf{M}_\perp$ plane, where $\mathbf{M}_\perp = \mathbf{B} \times (\mathbf{M} \times \mathbf{B})$ and \mathbf{N}_\perp is the direction perpendicular to \mathbf{B} and \mathbf{M}_\perp closely aligned with \mathbf{N} . The yellow and purple shaded regions indicate when MMS1 observed low-density electron beams and denser electron crescents, respectively.

density n_b by computing partial moments [8]. Throughout the yellow-shaded region the beam properties change somewhat, but without clear trends in position or time. The ratio n_b/n_e is ≈ 0.02 – 0.07 and the beam speeds are $v_b \approx [6\text{--}10] \times 10^3 \text{ km s}^{-1}$. In this region the bulk electron velocity \mathbf{V}_e and \mathbf{J} are small because n_b is small. In the purple-shaded region n_b/n_e increases from 0.1 to 0.3, and v_b decreases from $\approx 5 \times 10^3$ to $\approx 3 \times 10^3 \text{ km s}^{-1}$, as MMS1 approaches the X line. Here, a large $V_{\perp M}$ and $-J_M$ start to develop. These changes in n_b/n_e and v_b are responsible for the changes in

$A\phi_e/2$. All beam and crescent distributions propagate close to perpendicular to \mathbf{B} , primarily along the \mathbf{M} direction. Since $B_L < 0$ the source of the beams or crescents should be located in the $-\mathbf{N}$ direction, at the X line. The sharp reversal in B_L and large electron pressure divergence $\nabla \cdot \mathbf{P}_e$ may enable agyrotropic electron distributions to develop. At the X line $-\nabla \cdot \mathbf{P}_e/en_e$ peaks at $\approx 4 \text{ mV m}^{-1}$ in the \mathbf{N} direction based on four-spacecraft measurements (not shown), which may contribute to electron acceleration.

Large-amplitude high-frequency waves are observed at the same time as the agyrotropic electron beams at the boundary between the EDR and magnetosheath inflow region. Figures 2(d) and 2(e) show the waveform of the high-frequency \mathbf{E} parallel and perpendicular to \mathbf{B} and the spectrogram of \mathbf{E} . The wave power peaks close to $f_{pe} = 21 \text{ kHz}$. The wave \mathbf{E} is oblique to \mathbf{B} , so we identify the waves as UH waves. The amplitude peaks at $\approx 400 \text{ mV m}^{-1}$, an extremely large value, which approximately coincides with the maximum agyrotropy. The maximum wave energy density is $W_E = \epsilon_0 |\mathbf{E}|^2/2 \sim 7 \times 10^{-13} \text{ J m}^{-3}$, and the beam energy density is $W_b = m_e n_b v_b^2/2 \sim 5 \times 10^{-12} \text{ J m}^{-3}$. Therefore, $W_E \ll W_b$, consistent with the agyrotropic beam providing the free energy for the waves [10].

In Fig. 3 we investigate the properties of the UH waves in detail. Based on MVA of the waveform the wave has a well-defined maximum variance direction, shown in Fig. 3(a). The associated power spectrum [Fig. 3(d)] shows that the waves are centered around f_{pe} and have a relatively broad range of frequencies for UH or Langmuir-like waves. The hodograms of the waveform are shown in Figs. 3(b) and 3(c) in MVA coordinates, where E_{\min} , E_{\max} , and E_{int} are the electric fields in the minimum, maximum, and intermediate variance directions. They show that the waveform is one dimensional (1D) and linearly polarized, consistent with UH or Langmuir waves in a weakly magnetized plasma: $f_{pe}/f_{ce} = 63$ and $\rho_e/\lambda_D = 91$, where $f_{ce} = 340 \text{ Hz}$ is the electron cyclotron frequency, $\rho_e = 2 \text{ km}$, and $\lambda_D = 22 \text{ m}$. This suggests the waves are Langmuir-like, so we can assume the waves propagate in the E_{\max} direction. The ambiguity in the sign of the maximum variance direction is resolved by assuming the waves propagate in the direction closest to \mathbf{v}_b (justified below). The propagation direction is $\hat{\mathbf{k}} = [-0.65, 0.76, 0.06] (LMN)$, which is $\approx 80^\circ$ from \mathbf{B} .

Figures 3(e)–3(g) show the electron distributions in the $\mathbf{v}_{\perp 1} - \mathbf{v}_{\perp 2}$ plane, where $\mathbf{v}_{\perp 1}$ is along $\hat{\mathbf{k}} \times \mathbf{B}$ and $\mathbf{v}_{\perp 2}$ is along $\mathbf{B} \times (\hat{\mathbf{k}} \times \mathbf{B})$, which are observed simultaneously with the UH waves. The agyrotropic electron beams are closely aligned with $\hat{\mathbf{k}}$, consistent with the beam being responsible for the waves. No agyrotropic electrons are found in the $-\hat{\mathbf{k}}$ direction. The beam tends to broaden in the $\mathbf{v}_{\perp 1}$ direction and increase in density when the most intense waves

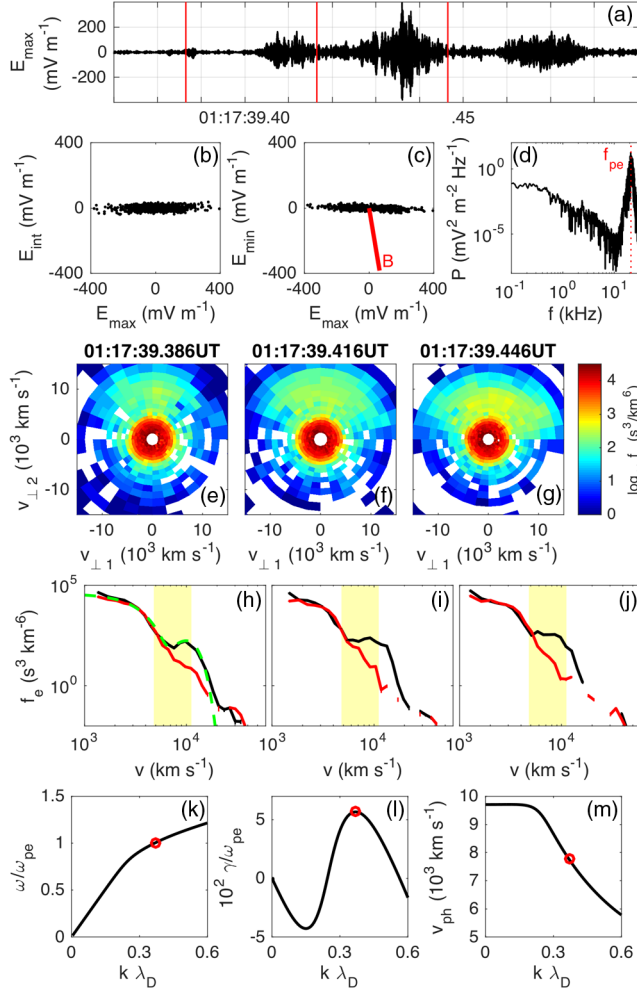


FIG. 3. UH waves observed by MMS1. (a) E_{\max} of the UH waves. (b),(c) Hodograms of E_{\max} versus E_{int} , and E_{\max} versus E_{\min} . The red line in (c) is the \mathbf{B} direction. (d) Power spectrum of E_{\max} (the red dashed line is f_{pe}). (e)–(g) Electron distributions in the $\mathbf{v}_{\perp 1} - \mathbf{v}_{\perp 2}$ plane at times indicated by the red vertical lines in panel (a). (h)–(j) 1D electron distributions along $\hat{\mathbf{k}}$ (black) and $-\hat{\mathbf{k}}$ (red) at times indicated by the red vertical lines in (a). The green dashed line in (h) is a two-Maxwellian fit to the black curve and the yellow shading indicates the domain of electron speeds trapped by the wave potential. (k)–(m) Frequency, γ , and v_{ph} of the unstable mode predicted from the fitted distribution in (h). The red circles indicate where γ is maximal.

are observed. This is possibly due to spatial changes in the beam density, but wave-particle interactions may also contribute to the evolution of the distribution. One-dimensional electron distributions from Figs. 3(e)–3(j) along $\hat{\mathbf{k}}$ and $-\hat{\mathbf{k}}$ are shown in Figs. 3(h)–3(j), respectively. Just before the large-amplitude waves are observed a clear electron beam is seen [Fig. 3(h)], indicating an unstable distribution. This beam is the only apparent energy source of the UH waves, so we conclude that the waves are driven by the beam. During the wave observations the

distributions develop a plateau [Figs. 3(i)–3(j)], suggestive of quasilinear relaxation. From Fig. 3(h) we estimate $v_b \approx 10^4 \text{ km s}^{-1}$ and the largest positive gradient in the electron distribution is at $v \approx 8 \times 10^3 \text{ km s}^{-1}$, which provides a good indicator of the wave's phase speed v_{ph} .

To investigate the wave properties further we calculate the properties of the unstable mode predicted by fitting two bi-Maxwellian distributions to the distribution in Fig. 3(h) assuming an unmagnetized plasma, and using $n_b/n_e = 0.02$ to agree with observations. At this time the wave amplitude is relatively small so we solve the linear dispersion equation. The unstable mode is predicted to be the beam mode [Figs. 3(k)–3(m)]. We note that for reduced n_b/n_e a growing Langmuir-like wave is found. Figure 3(l) shows that the mode has a maximum growth rate of $\gamma = 6 \times 10^{-2} \omega_{pe} \sim 4\Omega_{ce}$ for $f = f_{pe}$ [Fig. 3(k)]. Therefore, based on the linear growth rate the time required for the waves to grow to large amplitudes (of the order of the electron gyroperiod $\approx 3 \times 10^{-3} \text{ s}$) is well below the observation time of the agyrotropic electron beams ($\sim 0.3 \text{ s}$ on MMS1). The peak γ occurs at wave number $k\lambda_D \approx 0.35$, whence we calculate the wavelength $\lambda \approx 400 \text{ m} \approx 18\lambda_D$, which is much smaller than ρ_e and the electron beam gyroradius $\rho_b \approx 5 \text{ km}$. We predict $v_{ph} \approx 8 \times 10^3 \text{ km s}^{-1}$ [Fig. 3(m)], consistent with observations. Using this estimate of v_{ph} based on the waves with low amplitude and the linear dispersion relation, and E_{\max} from the observed high-amplitude waves, we estimate the maximum wave potential to be $\Phi \approx 30 \text{ V}$. These waves can trap electrons with speeds between $v_T = v_{ph} \pm \sqrt{2q_e\Phi/m_e} \approx [8 \pm 3.2] \times 10^3 \text{ km s}^{-1}$, which overlaps with most of the electron beam and part of the core in Fig. 3(h) and approximately spans the plateau in Figs. 3(i) and 3(j). Therefore, these waves are sufficiently large to account for the plateau distributions and can couple the agyrotropic beam to the core population, thus modifying the observed electron distributions. These wave-particle interactions may in turn increase \sqrt{Q} and $A\phi_e/2$ (both peak when the UH waves are observed), and hence modify the electron pressure tensor within the EDR.

Intense UH waves are also observed by MMS2 (Fig. 4), with peak amplitude $E_{\max} \approx 80 \text{ mV m}^{-1}$. The waveform is approximately 1D, with propagation direction $\hat{\mathbf{k}} = [-0.22, 0.96, -0.19]$ (LMN). Figures 4(b) and 4(c) show two adjacent electron distributions just before and during the UH wave observation. The agyrotropic beam is approximately perpendicular to \mathbf{B} and closely aligned with $\hat{\mathbf{k}}$. We estimate $n_b/n_e \approx 7 \times 10^{-3}$ and $v_b \approx 10^4 \text{ km s}^{-1}$, comparable to the MMS1 v_b , but a lower n_b . Overall, the observations confirm the results from MMS1 and suggest that UH wave generation occurs over volumes comparable to or larger than the spacecraft separation ($\sim 15 \text{ km}$).

This Letter shows the first observational evidence of electrostatic waves generated by agyrotropic electron beams produced by an EDR. We identify the largest

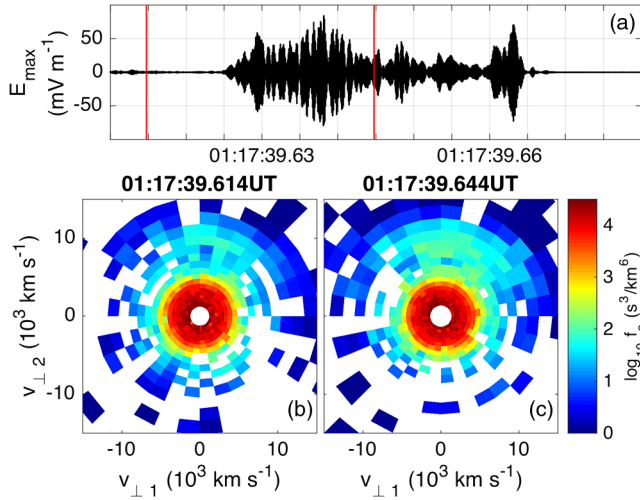


FIG. 4. UH waves observed by MMS2. (a) E_{\max} . (b),(c) Electron distributions in the $v_{\perp 1}$ - $v_{\perp 2}$ plane at times indicated by the red vertical lines in panel (a).

amplitude waves as UH waves and show that they are generated by electron beams propagating perpendicular to \mathbf{B} . The wave potentials are sufficiently large to scatter and thermalize the agyrotropic electrons and part of the core population. Therefore, the waves provide a source of electron diffusion, scattering, and heating near the EDR. The waves may even modify \mathbf{P}_e near the EDR, potentially influencing reconnection.

The observation of large-amplitude waves at the plasma frequency near the EDR means that EDRs can be viable sources of radio emission. For instance, Langmuir waves can be converted to electromagnetic waves via linear or nonlinear processes, e.g., linear-mode conversion [32], electromagnetic decay [33], electrostatic decay (or scattering off thermal ions) and coalescence [34,35], and antenna mechanisms associated with nonlinear currents [36]. The very large amplitude of the observed waves makes nonlinear processes possible. The agyrotropic electron beams can also directly generate electromagnetic waves, potentially becoming freely propagating radio waves [37,38]. The large density asymmetry often associated with asymmetric reconnection may also facilitate the escape of electromagnetic waves on the low-density side, enabling them to be detected remotely. Establishing the role of UH or Langmuir waves and agyrotropic electron beams produced at EDRs in generating electromagnetic emission is crucial for remote observations of magnetic reconnection, such as on the Sun's surface, where magnetic reconnection is associated with solar flares and coronal mass ejections, and in astrophysical plasmas [39].

MMS data are available by following the link in Ref. [40].

We thank the MMS team and instrument principle investigators for data access and support. This work was supported by the Swedish National Space Board, Grant No. 175/15.

- [1] E. R. Priest and T. Forbes, *Magnetic Reconnection: MHD Theory and Applications* (Cambridge University Press, Cambridge, England, 2000).
- [2] J. Scudder and W. Daughton, 'Illuminating' electron diffusion regions of collisionless magnetic reconnection using electron agyrotropy, *J. Geophys. Res.* **113**, A06222 (2008).
- [3] P. L. Pritchett and F. S. Mozer, Asymmetric magnetic reconnection in the presence of a guide field, *J. Geophys. Res.* **114**, A11210 (2009).
- [4] N. Aunai, M. Hesse, and M. Kuznetsova, Electron non-gyrotropy in the context of collisionless magnetic reconnection, *Phys. Plasmas* **20**, 092903 (2013).
- [5] M. Hesse, N. Aunai, D. Sibeck, and J. Birn, On the electron diffusion region in planar, asymmetric, systems, *Geophys. Res. Lett.* **41**, 8673 (2014).
- [6] L.-J. Chen, M. Hesse, S. Wang, N. Bessho, and W. Daughton, Electron energization and structure of the diffusion region during asymmetric reconnection, *Geophys. Res. Lett.* **43**, 2405 (2016).
- [7] J. L. Burch *et al.*, Electron-scale measurements of magnetic reconnection in space, *Science* **352**, 2939 (2016).
- [8] C. Norgren *et al.*, Finite gyroradius effects in the electron outflow of asymmetric magnetic reconnection, *Geophys. Res. Lett.* **43**, 6724 (2016).
- [9] W. M. Farrell, M. D. Desch, M. L. Kaiser, and K. Goetz, The dominance of electron plasma waves near a reconnection X-line region, *Geophys. Res. Lett.* **29**, 8-1 (2002).
- [10] W. M. Farrell, M. D. Desch, K. W. Ogilvie, M. L. Kaiser, and K. Goetz, The role of upper hybrid waves in magnetic reconnection, *Geophys. Res. Lett.* **30**, 2259 (2003).
- [11] A. Vaivads, M. André, S. C. Buchert, J.-E. Wahlund, A. N. Fazakerley, and N. Cornilleau-Wehrin, Cluster observations of lower hybrid turbulence within thin layers at the magnetopause, *Geophys. Res. Lett.* **31**, L03804 (2004).
- [12] M. Fujimoto, I. Shinohara, and H. Kojima, Reconnection and waves: A review with a perspective, *Space Sci. Rev.* **160**, 123 (2011).
- [13] X. Tang, C. Cattell, J. Dombeck, L. Dai, L. B. Wilson, III, A. Breneman, and A. Hupach, THEMIS observations of the magnetopause electron diffusion region: Large amplitude waves and heated electrons, *Geophys. Res. Lett.* **40**, 2884 (2013).
- [14] H. Viberg, Y. V. Khotyaintsev, A. Vaivads, M. André, and J. S. Pickett, Mapping HF waves in the reconnection diffusion region, *Geophys. Res. Lett.* **40**, 1032 (2013).
- [15] D. B. Graham, Y. V. Khotyaintsev, A. Vaivads, and M. André, Electrostatic solitary waves with distinct speeds associated with asymmetric reconnection, *Geophys. Res. Lett.* **42**, 215 (2015).
- [16] D. B. Graham, A. Vaivads, Y. V. Khotyaintsev, and M. André, Whistler emission in the separatrix regions of asymmetric reconnection, *J. Geophys. Res.* **121**, 1934 (2016).
- [17] Y. V. Khotyaintsev *et al.*, Electron jet of asymmetric reconnection, *Geophys. Res. Lett.* **43**, 5571 (2016).
- [18] D. B. Graham *et al.*, Lower hybrid waves in the ion diffusion and magnetospheric inflow regions, *J. Geophys. Res.: Space Phys.* **122**, 517 (2017).
- [19] J. Jara-Almonte, W. Daughton, and H. Ji, Debye scale turbulence within the electron diffusion layer during magnetic reconnection, *Phys. Plasmas* **21**, 032114 (2014).

- [20] J. L. Burch, T. E. Moore, R. B. Torbert, and B. L. Giles, Magnetospheric Multiscale overview and science objectives, *Space Sci. Rev.* **199**, 5 (2016).
- [21] R. E. Ergun *et al.*, Drift waves, intense parallel electric fields, and turbulence associated with asymmetric magnetic reconnection at the magnetopause, *Geophys. Res. Lett.* **44**, 2978 (2017).
- [22] L.-J. Chen, M. Hesse, S. Wang, D. Gershman, R. E. Ergun, J. Burch, N. Bessho, R. B. Torbert, B. Giles, J. Webster, C. Pollock, J. Dorelli, T. Moore, W. Paterson, B. Lavraud, R. Strangeway, C. Russell, Y. Khotyaintsev, P.-A. Lindqvist, and L. Avanov, Electron diffusion region during magnetopause reconnection with an intermediate guide field: Magnetospheric multiscale observations, *J. Geophys. Res. Space Phys.* **122**, 5235 (2017).
- [23] C. T. Russell *et al.*, The magnetospheric multiscale magnetometers, *Space Sci. Rev.* **199**, 189 (2016).
- [24] P.-A. Lindqvist *et al.*, The spin-plane double probe electric field instrument for MMS, *Space Sci. Rev.* **199**, 137 (2016).
- [25] R. E. Ergun *et al.*, The axial double probe and fields signal processing for the MMS mission, *Space Sci. Rev.* **199**, 167 (2016).
- [26] C. Pollock *et al.*, Fast plasma investigation for Magnetospheric Multiscale, *Space Sci. Rev.* **199**, 331 (2016).
- [27] D. B. Graham, Y. V. Khotyaintsev, A. Vaivads, M. André, and A. N. Fazakerley, Electron Dynamics in the Diffusion Region of an Asymmetric Magnetic Reconnection, *Phys. Rev. Lett.* **112**, 215004 (2014).
- [28] V. Roytershteyn, W. Daughton, H. Karimabadi, and F. S. Mozer, Influence of the Lower-Hybrid Drift Instability on Magnetic Reconnection in Asymmetric Configurations, *Phys. Rev. Lett.* **108**, 185001 (2012).
- [29] P. L. Pritchett, F. S. Mozer, and M. Wilber, Intense perpendicular electric fields associated with three-dimensional magnetic reconnection at the subsolar magnetopause, *J. Geophys. Res.* **117**, A06212 (2012).
- [30] D. B. Graham *et al.*, Electron currents and heating in the ion diffusion region of asymmetric reconnection, *Geophys. Res. Lett.* **43**, 4691 (2016).
- [31] M. Swisdak, Quantifying gyrotropy in magnetic reconnection, *Geophys. Res. Lett.* **43**, 43 (2016).
- [32] E.-H. Kim, I. H. Cairns, and P. A. Robinson, Extraordinary-Mode Radiation Produced by Linear-Mode Conversion of Langmuir Waves, *Phys. Rev. Lett.* **99**, 015003 (2007).
- [33] I. H. Cairns, Fundamental plasma emission involving ion sound waves, *J. Plasma Phys.* **38**, 169 (1987).
- [34] V. L. Ginzburg and V. V. Zhelezniakov, On the possible mechanisms of sporadic solar radio emission (radiation in an isotropic plasma), *Sov. Astron.* **2**, 653 (1958).
- [35] I. H. Cairns and D. B. Melrose, A theory for the 2fp radiation upstream of the Earth's bow shock, *J. Geophys. Res.* **90**, 6637 (1985).
- [36] D. M. Malaspina, I. H. Cairns, and R. E. Ergun, The 2f(p) radiation from localized Langmuir waves, *J. Geophys. Res.* **115**, A01101 (2010).
- [37] D. Tsiklauri, An alternative to the plasma emission model: Particle-in-cell, self-consistent electromagnetic wave emission simulations of solar type III radio bursts, *Phys. Plasmas* **18**, 052903 (2011).
- [38] H. Schmitz and D. Tsiklauri, The effect of initial conditions on the electromagnetic radiation generation in type III solar radio bursts, *Phys. Plasmas* **20**, 062903 (2013).
- [39] M. Yamada, R. Kulsrud, and H. Ji, Magnetic reconnection, *Rev. Mod. Phys.* **82**, 603 (2010).
- [40] See <https://lasp.colorado.edu/mms/sdc/public>.